energy&fuels

Article

pubs.acs.org/EF

Multiscale Description of Shale Pore Systems by Scanning SAXS and WAXS Microscopy

L. Leu,[*,†,‡] A. Georgiadis,[‡,§] M. J. Blunt,[†] A. Busch,[‡,¶] P. Bertier,[∥] K. Schweinar,[∥] M. Liebi,[⊥] A. Menzel,[⊥] and H. Ott[†,#]

[†]Department of Earth Science and Engineering, Imperial College London, SW7 2BP, U.K.

[‡]Shell Global Solutions International B.V., Kessler Park 1, 2288 GS Rijswijk, The Netherlands

[§]Department of Chemical Engineering, Imperial College London, SW7 2AZ, U.K.

[∥]Clay and Interface Mineralogy, RWTH, Aachen 52062 , Germany

[⊥]Paul Scherrer Institut, Swiss Light Source, 5232 Villigen, Switzerland

[#]Department of Petroleum Engineering, Montanuniversität, Leoben 8700, Austria

[¶]Lyell Centre for Marine and Earth Science and Technology, Heriot-Watt University, EH14 4AP Edinburgh, U.K.

ABSTRACT: The pore space of shales and mudrocks ranges from molecular dimensions to micrometers in length scale. This leads to great variation in spatial characteristics across many orders of magnitude, which poses a challenge for the determination of a representative microscopic pore network for such systems. Standard characterization techniques generally provide volume-averaged properties while high-resolution imaging techniques do not assess a representative range of pore sizes because of limitations in the spatial resolution over the field of view. Due to this complexity, open questions remain regarding the role of the pore network in retention and transport processes, which in turn control oil and gas production. Volume-averaged but spatially resolved information is obtained for pores of size from 2 to 150 nm by applying scanning small- and wide-angle X-ray scattering (SAXS and WAXS) microscopy. Scattering patterns are collected in a scanning microscopy mode, such that microvoxels are sampled sequentially, over a total of 2×2 mm^2 raster area on specifically prepared thin sections with a thickness of 10−30 μm. Spatially resolved variations of porosity, pore-size distribution, orientation, as well as mineralogy are derived simultaneously. Aiming at a full characterization of the shale pore network, the measurements and subsequent matrix porosity analysis are integrated in a multiscale imaging workflow involving FIB-SEM, SEM, and μ-CT analysis.

1. INTRODUCTION

Large-scale shale and mudrock formations are considered as seals for trapping hydrocarbons, for permanent or temporal (carbon dioxide, methane, or hydrogen) gas storage, for nuclear waste storage, and as source or reservoir rock for hydrocarbons. Fluid transport in geological reservoirs occurs over different length scales, ranging from the pore- to the field-scale, and is determined by effects over all these different regimes.[1] While large-scale fractures create fast flow pathways, matrix properties sustain fluid supply, governed by diffusion, matrix porosity, gas oil and water adsorption/desorption, and other transport.[1] Thus, prediction of pore scale flow and transport in shales has significant implications in reservoir productivity and long-term integrity predictions. To model such diverse transport phenomena, a virtual transport network must be extracted from the physical rock. This network must capture the representative pore structure.[2] An accurate digital rock model thus relies on a detailed characterization of the pore system.

This pore space characterization is a complex task, because shales exhibit broad mineralogical and structural heterogeneity over many length scales. There is a complex arrangement of pores in terms of size and distribution as well as orientation, which ultimately controls flow and transport. Pores in shale range from a few angstroms up to several micrometers in size.[3] The largest pores (>50 nm) fall under the category of macropores whereas smaller pores are classified as micro- (<2 nm) or meso- (2−50 nm) pores, according to the IUPAC classification scheme.[4] Pores may occur in contact areas between grains or minerals, i.e. pyrite crystals, or between clay mineral aggregates and platelets. However, they may also be inherent to components of the rock, such as fossils, or organic matter.[5] Pores can then be distributed heterogeneously in number, volume, and space.[6−8] In particular, micro- and mesopores, largely connected to clay minerals and within organic matter, can be highly abundant. Because of their high internal surface area and abundance, such pores can dominate gas sorption processes.[1,9−12] Micro- and mesopores may thus contain a large proportion of the total gas in place for gas shales.[10] Furthermore, micro- and mesopores may connect larger pores,[13] permitting flow. The majority of the pores in the shale matrix are aligned subparallel to the bedding plane because of preferred mineral and particle orientation.[14] This structural anisotropy leads to anisotropy of flow and mechanical properties.[15−17] Pores associated with specific minerals or components of the rock may impact flow and transport processes differently, depending on their number, size, and location.[18] However, assessing and quantifying a wide range of parameters, such as size, distribution, location, and orientation

Received: September 7, 2016
Revised: October 31, 2016
Published: November 2, 2016

DOI: 10.1021/acs.energyfuels.6b02256
Energy Fuels XXXX, XXX, XXX−XXX

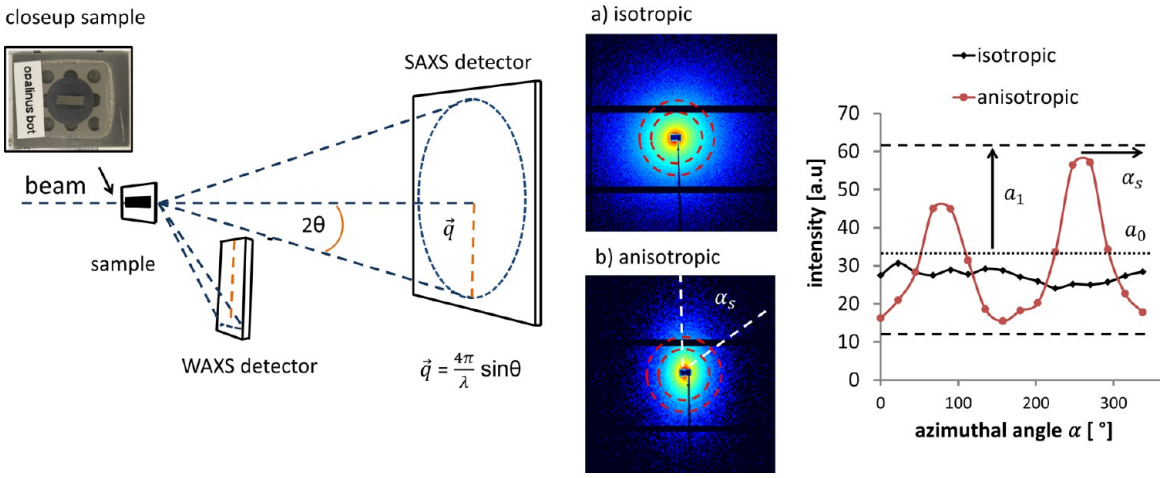

Figure 1. Principle of small- and wide-angle scattering and the experimental apparatus. Passing through the porous sample, X-rays are scattered to small and wide angles with the scattering angle 2θ. The intensity distribution is measured as a function of scattering vector $q = \frac{4\pi}{\lambda} \sin\theta$on two area detectors behind the sample. The scattered intensity was integrated radially for isotropic (a) and anisotropic (b) scattering structures over a q range covering an area indicated by the red dotted lines. From the resulting average intensity dependence on azimuthal angle plot, the different orientation parameters—the average scattering intensity, the anisotropic intensity, and orientation angle a_0, a_1, and α_s—can be extracted.

of pores, and minerals over the different relevant scales is challenging for analytical methods.

Imaging techniques can quantify local porosity and pore-size distributions,[7,8,19] pore orientation, and connectivity,[20] as well as 2D and 3D mineral and pore configuration.[21] Each imaging technique focuses on a respective size range, yielding a suite of different methods, including μ-CT, BIB-SEM, FIB-SEM, TEM, AFM, and helium ion microscopy.[21−24] Because some methods have partially overlapping accessible size ranges, they can be combined in a multiscale imaging approach to extract information over the entire pore-size range.[25] The major drawback of imaging methods, however, is the inevitable trade-off between resolution and field of view: the higher the imaging resolution, the smaller the field of view. As a result, the assessed sample volumes become microscopic for the highest resolution images, which are needed to detect micro- and mesopores. For shales with significant spatial heterogeneity, the image may not be representative of the average rock structure.[13]

An alternative way of probing statistically representative pore-scale information for shales is through the application of fluid invasion and radiation measurement techniques.[26] For example, two of the most commonly applied fluid invasion techniques are mercury injection capillary pressure (MICP) and low-pressure gas adsorption of nitrogen or carbon dioxide. Each method has benefits in the application on shales, discussed in more detail in the literature.[26,27] Even though both MICP and low pressure gas adsorption give valuable pore-scale information, they are limited to a specific size range that does not cover the entire pore range and they do not provide spatially resolved information.

Small-angle scattering methods such as (ultra) small-angle neutron or X-ray scattering (USANS/USAXS) can assess the size range from several angstroms up to several micrometers, which encompasses almost all the pore sizes seen in shales. (U)SANS[3,17,23,26,28−32] but also USAXS[33] have been applied on different shales to measure porosity and pore-size and surface-area distributions.

Small-angle scattering can also measure the orientation of structures within a variety of different materials,[34−37] including pores in shale.[17,38] The average degree of orientation and the orientation angle of the scattering can be quantified for the targeted sample volume.

In shales, the orientation angle is a direct measure of the average direction that the majority of pores are facing, whereas the degree of orientation is a measure of the tendency of pores to either face the same way or be randomly distributed. Pore orientation in shales causes anisotropy in the flow and transport processes, and therefore both parameters are closely related to the mechanical and flow properties of the rock.[17] Strong pore orientation may be found in small-angle scattering experiments on shales when the sample is cut perpendicular to bedding. The reason is that pores in shales are usually oriented subparallel to bedding, without any preferential orientation within the bedding plane. As opposed to imaging methods, SANS can be applied to quantify the volume, distribution, and average orientation of the smallest pores in statistically representative sample volumes. However, imaging methods provide a significantly higher level of detail through resolving the sizes and shapes of each pore individually.

Neutron sources generally have low fluxes, and neutrons are less likely to scatter than X-rays. To achieve reasonable counting statistics in a SANS experiment, the neutron beam is focused over several square millimeters. Therefore, USANS typically probes volumes of a few cubic millimeters, which is several orders of magnitude bigger than the microscopic structural heterogeneity of shale. As a consequence, it is difficult to resolve and determine component-specific variations of porosity, pore-size distribution, and pore orientation. It is then challenging to directly quantify the amount of organic versus inorganic matter, and fossil porosity out of the total measured porosity. This means that neither SANS nor imaging methods are most suitable to directly measure component-specific micro- and mesopores for statistically relevant sample volumes.

Due to high photon flux at synchrotron sources, the application of X-rays instead allows a considerable beam size reduction, resulting in a smaller scanning volume. Therefore, the SAXS spot size can be focused[39] to several square micrometers, allowing localized SAXS measurements. Such measurements are common in biology.[35,37] The main interest is to resolve the local variation of the orientation of ordered

DOI: 10.1021/acs.energyfuels.6b02256
Energy Fuels XXXX, XXX, XXX−XXX

nanoscopic structures, such as muscular fibrils[35] or bone fibers.[37] These measurements are often performed sequentially across large sample areas to determine local variations in properties. Furthermore, the measurements are often combined with wide-angle X-ray scattering (WAXS), which gives complementary information to SAXS, assessing features <1 nm. The method can therefore be used to identify minerals and crystal orientation.[37] On shales, single synchrotron WAXS measurements were performed to study average mineralogy and preferred mineral orientation.[16,40] However, localized SAXS-WAXS measurements with a microscopic beam size have not been performed on shale as of yet.

In this study we apply synchrotron scanning SAXS-WAXS microscopy on shales. We use small-angle scattering to obtain localized scattering information on the micro-, meso-, and macropores. A key aspect of the experiment is that the beam size is microscopic, such that the probed volumes approach the physical size of the structural heterogeneity of the rock. Simultaneously, consecutive SAXS and WAXS patterns are recorded over a square millimeter raster, also providing sufficient sampling statistics. Local porosity, pore-size distribution, and pore orientation as well as mineralogy are quantified, together with their spatial variability. The results are benchmarked against SANS and nitrogen adsorption measurements from twin samples. Finally, we combine and integrate small-angle scattering in an imaging workflow including FIB-SEM, SEM/EDX, and μ-CT to assess the full pore-size range. We register all data such that imaging and scattering can be directly combined, serving the larger scope of this work, which is to determine the pore structure to use as input for modeling and flow predictions.

1.1. Scattering methods and the pore network. The experimental technique applied in this work makes use of several aspects of small- and wide-angle scattering. SAXS/SANS and WAXS resolve structural features ranging from several angstroms to tens of micrometers in size. A representative experiment is shown in Figure 1.

The X-ray beam is directed toward the sample, after which a proportion of the photons are elastically scattered at an angle. This scattering process is caused by variations of the scattering length density (SLD) within the path of the beam. For SAXS this means that the scattering is predominantly caused by pores and a rock matrix that have a high contrast in SLD. The scattered photon intensity is then captured as a 2D scattering pattern on an area detector located at a specified distance behind the sample (Figure 1). The scattered photon intensity is measured as a function of the scattering vector q given by

$$q = \frac{4\pi}{\lambda}\sin\theta = \frac{2\pi}{d} \tag{1}$$

where λ is the photon wavelength, 2θ is the scattering angle between incoming and scattered radiation, and d is the characteristic real size of a scattering object. So, with the relationship $d \approx \frac{2\pi}{q}$ the pore diameter can be approximated for a specific q at the detector. It follows that small pores scatter photons to large angles and hence larger q, whereas large pores scatter to smaller angles and q. For most applications, the measured scattered intensity distribution is averaged over the detector area and presented as an intensity I versus q plot. $I(q)$ may then be interpreted with respect to the size and distribution of pores in the sample.

An important element in the interpretation of SAXS data is the SLD calculation of the individual components of the sample, as this affects the scattering intensity. For a specific mineral phase j, the SLD, ρ_j^*, is determined by[38]

$$\rho_j^* = \rho_j N_a \sum_{i=1}^{n} \frac{Z_i b_0}{M_i} \tag{2}$$

where ρ_j is the density of phase j, N_a is Avogadro's number, n is the number of atoms in the molecule comprising phase j, Z_i and M_i are the atomic number and mass of each atom, respectively, and $b_0 = 2.82 \times 10^{-13}$ cm is the Thompson scattering factor. As the scattering length of neutrons is independent of Z, in SANS, $Z_i b_0$ is replaced by the coherent scattering length b_i of every ith element.

Shales contain several mineral phases whose variations in SLD cause scattering. However, the SLD contrast between the individual minerals is generally much weaker than that with air. Therefore, it is common practice to use an average SLD calculation for the mineral matrix, including the organic matter.[41,42] This is done so that a two-phase system can be assumed, which is often required for the interpretation of SAXS data. We therefore define an average matrix SLD as

$$\rho^* = \frac{\sum_{j=1}^{m} V_j \rho_j^*}{\sum_{j=1}^{m} V_j} \tag{3}$$

where $j = 1, m$ are the individual phases present in the matrix volume V_j with their respective ρ_j^*. As discussed by Anovitz and Cole,[42] this averaging may introduce a significant error when there are large differences in the SLD values of different phases. For SANS, this could be hydrogen-bearing phases with a high percentage of low mature and thus hydrogen-rich kerogen. For SAXS this could be heavy oxides. However, in terms of data analysis, assuming a three-phase system significantly increases the complexity for the quantification[43] and is not done here.

A widely used approach to retrieve pore-size distributions, surface area, and porosity from SAXS measurements uses the polydisperse spheres model.[44] It assumes the rock to be a two-phase system comprising a mineral matrix and pores. It further assumes a random orientation and spherical shape of pores, distributed in size following a power law. For a system of polydisperse randomly oriented spheres, the scattered intensity can then analytically be expressed as[45,46]

$$I(q) = (\rho^* - \rho_{air}^*)^2 \frac{\varphi}{\overline{V_r}} \int_{R_{\min}}^{R_{\max}} V_r^2 f(r) F_{sph}(qr)\, \mathrm{d}r \tag{4}$$

where $\rho^* - \rho_{air}^*$ is the contrast of the SLDs between matrix and air, φ is the porosity, $\overline{V_r} = \int_0^\infty V_r f(r)\, \mathrm{d}r$ the average pore volume, following the respective pore-size distribution probability function $f(r)$, and $F_{sph}(qr)$ is the form factor, which defines the role of particle shape in scattering profiles, here considered to be that of solid spheres.[45,46] The model we use to determine $f(r)$ is implemented in the PRINSAS software, as explained in more detail by Hinde[45] or Radlinski.[46] As input, the model requires the experimental $I(q)$ and calculated SLD for the mineral matrix. It then fits $I(q)$ to retrieve $f(r)$.

We also use SAXS to quantify the average pore orientation. The anisotropy of the scattering pattern can be caused by preferential orientation of particles (here pores) in the scattering volume.[36] This means that the pattern becomes more elliptic with increasing degree of preferential orientation.

DOI: 10.1021/acs.energyfuels.6b02256
Energy Fuels XXXX, XXX, XXX−XXX

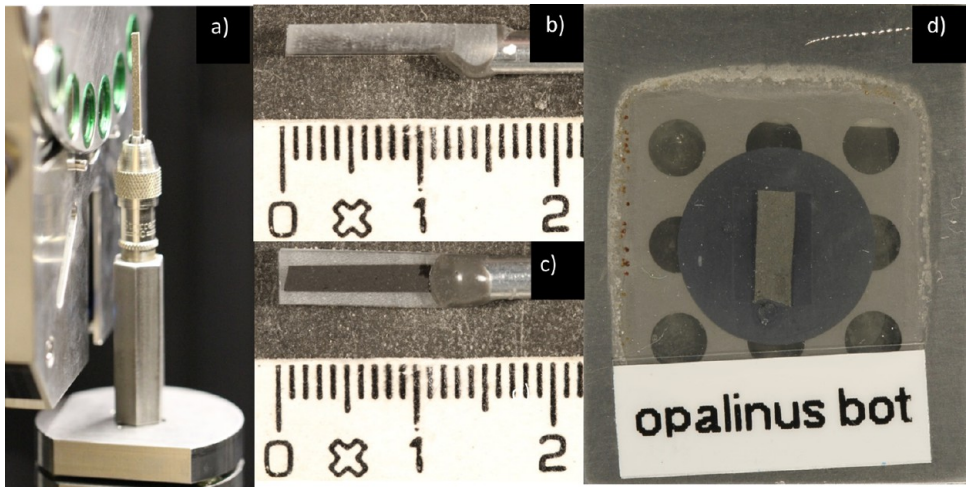

Figure 2. Sample preparation overview: (a) $2 \times 2 \times 20$ mm^3 rectangular segments are μ-CT scanned. (b, c) The sample is subsequently embedded in resin, bisected, polished, and rescanned, and (d) mounted on a Si-wafer or Capton foil substrate and sample holder, polished to a thickness of approximately 10 or 30 μm, and then used for scanning SAXS-WAXS microscopy.

In addition, the orientation of the scattering pattern corresponds to the actual orientation of the particles but 90 deg rotated in terms of the long axis of the pattern (in a plane perpendicular to the beam). To capture this anisotropy, the radial averaging of the intensity distribution over the detector as a function of azimuthal angle α is analyzed. Commonly, radial averaging is applied to reduce the 2D scattered intensity distribution to an $I(q)$ plot for further analysis. However, in such a case, information on the anisotropy is averaged out and, hence, the intensity distribution of a specific q is represented by a single average value. Therefore, in the present study, the detector is subdivided into $N_\alpha = 16$ segments, each covering an azimuthal range of 22.5°, for which each a radial integration is performed.[35] The resulting average intensity distribution for a specific q range is fitted assuming a sinusoidal form:[35]

$$I(n_\alpha) \approx a_0 + a_1 \cos\left(\frac{2\pi n_\alpha}{N_\alpha} - \alpha_s\right) \tag{5}$$

where a_0 and a_1 are the average and oriented intensities, respectively, α_s the orientation angle, n_α the azimuthal segment, and N_α the total azimuthal segments.

In Figure 1 we show two examples of experimental scattering patterns which illustrate the process, plotting the average intensity distribution versus the azimuthal angle of two different samples. The data are from two measurements: one of a random oriented pore structure (a); and one from an oriented structure (b). From (a), no clear orientation can be derived; hence, the scattering pattern is rather spherical. Consequently, the average intensity does not vary much with azimuthal angle. However, in (b), the average intensity shows sinusoidal dependence on azimuthal angle. All parameters a_0, a_1, and α_s can be extracted as indicated for structure b. In addition, the degree of orientation can be defined as a_1/a_0. It follows that for each measurement also the degree and orientation angle of the pores can be quantified (note that the average pore orientation is 90° rotated to the long axis of the scattering pattern).

From WAXS data different aspects of mineralogy can be quantified. When applied to shales, the radially integrated pattern displays strong intensity maxima for a given q. For historic reasons, in the diffraction community the intensity is given as a function of scattering angle (2θ) instead of the scattering vector q. In this study this terminology is therefore applied to WAXS measurements. Similar to SAXS, each peak position corresponds to a characteristic length in the WAXS measurements. For the size range covered with WAXS, these are atomic distances in a crystal lattice. Each mineral thus has a characteristic combination of peaks in the scattering pattern, corresponding to its crystal structure. While different minerals may show overlapping peaks, other single peaks may be indicative for a specific mineral. Minerals can thus be identified by finding mineral characteristic peak combinations in the scattering pattern.

2. MATERIALS AND METHODS

2.1. Samples and sample preparation. The rock types used were selected to represent a large variety of structural differences, comprising Opalinus Clay, oil shale from Jordan, and a schist from France. The Opalinus Clay sample represents an organic lean shale sample. For this specific sample, details can be found in Busch et al. (2016), referenced therein as CCP 14.[26,27,32] The Cretaceous-Eocene oil shale here referred to as Jordan shale was not buried deeply, therefore no strong orientation of the pores is expected; more details about the core can be found in Alqudah et al.[47] The last rock sample is low-grade metamorphic schist from an outcrop in the Loire valley in France. This Anjou black schist, referred to here as France shale, is expected to have the highest degree of pore alignment.

Samples were initially trimmed from core pieces to $2 \times 2 \times 20$ mm^3 rectangular segments which were scanned using μ-CT; see Figure 2. Following that, the samples were embedded in resin and were bisected along their length (Figure 2 b). The new exposed surfaces were then polished, and additional μ-CT tomograms were obtained for both new segments. These were then mounted on a rigid perforated steel frame, supported by a substrate, with which their polished surfaces were contacted in permanent adhesion. Two material options were tested as substrates, aiming at minimal scattering interference: Kapton foil, and monocrystalline Si wafers of 001 orientation and 50 μm thickness. After mounting the samples onto the substrate and frame, they were polished, without water, to a thickness of 10 or 30 μm thin sections. An example for a final thin section as it was used for SAXS-WAXS microscopy is shown in Figure 2(d).

Table 1 summarizes at which orientation each sample was cut with respect to bedding, including details of sample preparation along with expected features due to geologic history and chemical composition.

2.2. Experimental settings for multiscale Imaging, SAXS, and SANS. μ-CT scans were performed with an XRADIA Versa 520, operated at 50 keV 5 W, with a voxel size of 1 μm. The FIB-SEM

DOI: 10.1021/acs.energyfuels.6b02256
Energy Fuels XXXX, XXX, XXX−XXX

Table 1. Overview of the Samples' Thin Section Orientation with Respect to Bedding and Expected Features

Sample name	Section orientation with respect to bedding: Perpendicular	Section orientation with respect to bedding: Parallel	Features
Opalinus		√	Organic lean
Jordan	√	√	High porosity, low degree of orientation
France	√		Low porosity, high degree of orientation

imaging was performed with a Helios 600 Nanolab Dual Beam instrument from FEI on a carbon-coated thin section. In the slice and view mode, serial images were collected from two volumes. The images were obtained at 1 kV with a 0.69 nA spot size and exposure time of 60 μs. The in lens-detector was at a 38° angle, perpendicular to the milling surface. For the milling with a Ga^+ ion beam, nominal 10 nm steps were used, resulting in two different volumes of 10.3 μm horizontal and 8.9 μm vertical width and 6.3 μm depth, resulting in 499 and 550 frames for volumes 1 and 2 respectively.

The scanning SAXS-WAXS microscopy was performed at the cSAXS beamline of the Swiss Light Source (SLS) at the Paul Scherrer Institute, Switzerland. The experiments were performed with a monochromatic synchrotron beam of 12.4 or 11.2 keV photon energy. The beam was focused to a spot size of 10 × 25 μm^2 and a scanning range of either 2 × 2 or 1.5 × 2.75 mm^2, respectively. The step size in the x and y directions for lateral scanning was 10 μm. Because the physical beam size is 10 × 25 μm^2, the SAXS pattern contains overlapping scattering information in the vertical direction. The SAXS patterns were recorded on a Pilatus 2 M detector with a pixel size of 0.172 mm at a sample−detector distance of 7.1 or 6.096 m, respectively, resolving a q range of about 0.0016−0.17 Å^{-1} and 0.001−0.14 Å^{-1}, respectively. The exposure time was 0.04 s. The WAXS patterns were recorded on a Pilatus 300 K detector with a pixel size of 0.172 mm, capturing a fraction of less than 8° of the full angular range of the entire scattering pattern. The sample detector distance was 630.5 mm resolving a q range of 0.4−2.6 Å^{-1} and an angular range of 2θ = 4−37°.

SANS and USANS data were obtained at KWS 1 and KWS3, respectively, at Heinz-Meier-Leibnitz Zentrum (MLZ) in Garching, Germany, operated by the Jülich Center for Neutron Science (JCNS).[26] Data at KWS-1 were collected at a wavelength of λ of 0.6 nm with a wavelength distribution of the velocity selector $\frac{\Delta\lambda}{\lambda}$ = 0.10 (full width at half-maximum). Measurements were performed at sample-to-detector distances of 19.7 m, 7.7 m, and 1.2 m, covering a q range of 0.002−0.35 Å^{-1}. Data at KWS-3 were collected at λ = 1.28 nm, $\frac{\Delta\lambda}{\lambda}$ = 0.2, and a sample-to-detector distance of 9.5 m, covering a q range from 0.0024 to 0.00016 Å^{-1}. Hence, pore diameters for the combined SANS and VSANS measurements range between $d \approx \frac{2\pi}{q}$= 1.75 nm and 3 μm. Further details of the measurement procedure and sample description are given by Busch et al.[26]

2.3. Data treatment. The orientation analysis for the SAXS data was performed using Matlab macros available at the cSAXS beamline and downloadable at ref 48. The scripts are tailored for the analysis of scanning SAXS-WAXS data. In the first step for every measurement point, a separate data analysis is performed using eq 5 to calculate the average intensity a_0, the oriented intensity a_1, and the orientation angle α_s. The script generates maps showing the distribution of these properties. In addition, maps are generated with the degree of orientation a_1/a_0, the average and oriented intensity and orientation angles a_0,a_1, and α_s, and the intensity exponent.

The quantitative data for porosity and pore-size distributions that will be discussed are from Opalinus Clay. For the specific sample a suite of experimental reference data is available including XRD, SANS, and N_2 sorption data.[26] In this study we use the reported XRD data, N_2 sorption data, and SANS data, to compare to SAXS and WAXS results from cSAXS.

Based on the reported mineralogy, the structural formula, and the density shown in Table 2, for every mineral the SLD was calculated based on eq 2. Then an average SLD of the individual contributions for the mineral matrix is calculated using eq 3. The calculations were done with the scattering length density calculator in the software SASfit[49] for both SANS and SAXS data. Input parameters for the individual calculation are based on mineralogical formulas, mass density ρ, an X-ray energy of 11.2 keV, and a neutron wavelength of 0.6 nm, as shown in Table 2. Samples used for SAXS, as well as twin samples for N2 adsorption and SANS measurements, were drilled from different locations of the same core piece measuring approximately 2 cm in height and 4 cm in diameter.[26]

USANS and SANS data were calibrated by means of absolute scattering cross-section by using an internal Perspex standard. With the help of a standard of known scattering behavior, a parameter is determined to shift the measured $I(q)$ in magnitude. This step is necessary for quantitative data analysis. Lacking experimental absolute calibration for SAXS data, we followed the approach by Zhang et al.[50] for intercalibrating SANS and SAXS data. From SANS measurements conducted on twin samples of Opalinus Clay, the expected $I(q)$ was calculated for the experimental conditions at cSAXS. The calculation is based on the square of the ratio of the average X-ray and neutron SLD for the rock matrix (Table 2):

Table 2. Average Neutron and X-ray SLD Calculated for the Given Experimental Settings Based on Average Rock Mineralogy Obtained from Busch et al.[26]

Mineral	structural formula	density [g/cm^3]	fraction	neutron SLD [cm^{-2}]	X-ray SLD at 11.2 keV [cm^{-2}]
Quartz	SiO_2	2.65	0.142	4.18×10^{10}	2.26×10^{11}
Albite	$NaAlSi_3O_8$	2.62	0.014	3.97×10^{10}	2.218×10^{11}
K-Feldspar	$KAlSi_3O_8$	2.56	0.020	3.66×10^{10}	2.171×10^{11}
Kaolinite	$Al_2Si_2O_5(OH)_4$	2.63	0.213	3.22×10^{10}	2.261×10^{11}
Illite	$K_{0.65}Al_{2.0}Al_{0.65}Si_{3.35}O_{10}(OH)_2$	2.75	0.475	3.77×10^{10}	2.339×10^{11}
Chlorite	$Fe_{3.5}Mg_{1.5}Al(Si_3Al)O_{10}(OH)$	3.2	0.046	3.91×10^{10}	2.696×10^{11}
Calcite	$CaCO_3$	2.71	0.041	4.69×10^{10}	2.316×10^{11}
Dolomite	$CaMg(CO_3)_2$	2.88	0.004	5.97×10^{10}	2.452×10^{11}
Siderite	$FeCO_3$	3.96	0.008	6.90×10^{10}	3.26×10^{11}
Pyrite	FeS_2	5.01	0.010	3.81×10^{10}	4.149×10^{11}
Anhydrite	$CaSO_4$	2.98	0.009	4.05×10^{10}	2.549×10^{11}
Gypsum	$CaSO_4 \times 2(H_2O)$	2.31	0.006	2.21×10^{10}	2.019×10^{11}
TOC	CH	1.3	0.012	1.75×10^{10}	1.187×10^{11}
Average		2.89	1	3.76×10^{10}	2.33×10^{11}

DOI: 10.1021/acs.energyfuels.6b02256
Energy Fuels XXXX, XXX, XXX−XXX

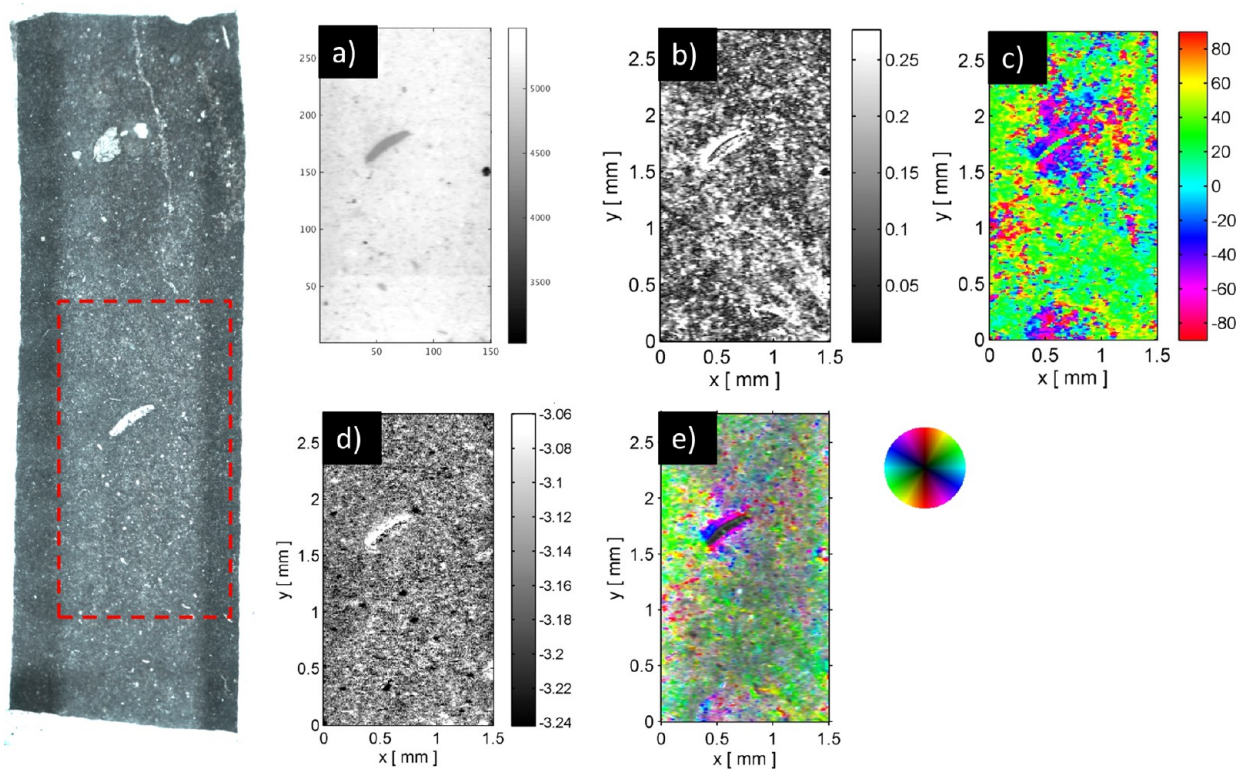

Figure 3. Data from the SAXS microscopy analysis performed on Opalinus Clay. The microscopic image on the left indicates the scanning area framed by a red dotted line. Image (a) shows the adsorption map (X-ray microscope), where the microscopic grains and matrix can be identified. (b) shows the degree of orientation, with stronger local variation of the degree of orientation around a large mineral grain in the center of the image. In (c) the angle of the main scattering on a plane perpendicular to the beam is shown. The direction of the axis representing the scattering orientation is color-coded in degrees and is 90° rotated to the real average orientation of pores in the same plane. The orientation distribution seems to be random. (d) shows the intensity exponent, varying from 3.06 to 3.24. The orientation angle with asymmetric and symmetric scattering intensity shown in map (e) suggests that the mineral grain in the center is significantly less porous than the area around this grain. The scan area is approximately 2 × 2 mm^2; each of the 40,000 pixels is 10 × 10 μm^2, containing scattering information over 25 × 10 × 30 μm^3.

$$I_{SAXS,expected}(q) = I_{SANS}(q) \times \frac{(SLD_{average,X\text{-}rays})^2}{(SLD_{average,neutrons})^2} \quad (6)$$

where $I_{SAXS,expected}(q)$ is the expected curve from the measured SANS curve $I_{SANS}(q)$, and $SLD_{average,\ X\text{-}rays}$ and $SLD_{average,\ neutrons}$ are the average SLD for the rock matrix for X-rays and neutrons, respectively.

In the next step, a shifting parameter is determined for the experimental transmission corrected SAXS data on Opalinus Clay. First, the average $I(q)$ of the experimental SAXS data (the green area in Figure 6(a)) is manually shifted to fit the expected SAXS curve $I_{SAXS,expected}(q)$, yielding a shifting parameter. In the following, the shift parameter is then applied to each single measurement. The explicit assumption here is that the microstructures of the sample analyzed with SANS and average SAXS are identical. In that case $I_{SAXS,expected}(q)$ and the average SAXS $I(q)$ can be superimposed. We make the assumption based on results by Busch et al.[26] showing that twin samples of the same rock sample have a similar scattering behavior. We expect little variation; hence, we perform the SAXS measurements on a twin sample of the exact same material. An uncertainty of unknown magnitude may be introduced by this scaling. It should, however, not affect the relative intensities measured from individual SAXS volumes.

The calibrated $I(q)$ values from SANS and SAXS were fitted with the PRINSAS software[45] applying the polydisperse spheres model. An average SLD for the matrix was required for SAXS and SANS for the fit. The average SLDs used are reported in Table 2. The fit returned $f(r)$ as a function of pore radius for SAXS and SANS. Porosities were obtained by summing the pore volume and dividing by the sample volume. Respective pore-size distributions from SANS and SAXS patterns are compared to each other and to N_2 sorption data[26] as cumulative pore volume distributions versus (pore) radius.

Characteristic minerals were identified in the WAXS patterns via peak fitting of the expected patterns to the experimental data. Possible minerals and the expected scattering pattern for each mineral were obtained from Rietvelt refined XRD data for Opalinus Clay.[26]

Image processing of the FIB-SEM and μ-CT data, as well as image registration of FIB-SEM, SEM/EDX, μ-CT, and SAXS data was performed in the Avizo[51] software. The image processing involved image filtering using a nonlocal means filter and a watershed-based segmentation. For the image registration in Avizo, in the first step a rough "by eye" registration is performed, followed by an automated iterative method using the image registration module.

3. RESULTS AND DISCUSSION

3.1. Section description. In this section we present the experimental results subdivided into six subsections. The general purpose and content of each section is summarized below.

- Section 3.2 shows the variety of results from the scanning SAXS-WAXS microscopy measurements at cSAXS. The main purpose is to demonstrate the information content that is available. The rock investigated first is Opalinus Clay, cut parallel to bedding. The same rock will be further investigated in Section 3.4. The results show the different parameters as a function of position in the sample.
- Section 3.3 provides an orientation analysis on rocks perpendicular to the bedding plane, where the effects of anisotropy are expected to be more marked. Jordan shale

DOI: 10.1021/acs.energyfuels.6b02256
Energy Fuels XXXX, XXX, XXX−XXX

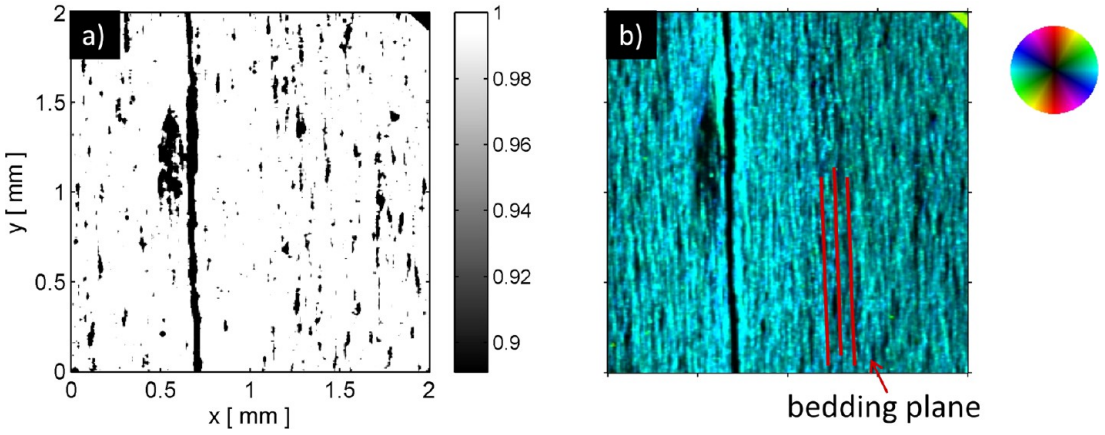

Figure 4. (a) Degree of orientation. (b) Asymmetric and symmetric scattering intensity for France shale measured perpendicular to bedding. The degree of orientation (a) is high, indicating a preferential orientation of pores. A large vein in the center displays a lower degree of orientation, indicating that the values vary locally. The average orientation of pores shown in (b) is subparallel to bedding. Local differences in the scattering intensity can be seen where dark colors indicate fewer pores. Low porosity and low degree of orientation seem to be connected to micrometer-sized mineral grains.

and France shale are compared. Both have a different burial history and, therefore, show differences in the magnitude of the degree of orientation.

- Section 3.4 presents the volumetric properties that were modeled from the SAXS data of Opalinus Clay. Individual small SAXS volumes are selected, analyzed, and compared. The measurements target the rock matrix, the contact area of the matrix, and large minerals. The data is compared to N_2 and SANS results to validate the SAXS data.
- Section 3.5 presents WAXS results for Opalinus Clay. The purpose is to identify minerals from the scattering pattern.
- Section 3.6 shows the combination of imaging and scattering for the same Opalinus Clay sample that was used in the previous sections. First it is demonstrated that μ-CT SEM and scanning SAXS-WAXS can be combined. Then we register FIB-SEM volumes to the scattering data.
- Section 3.7 is a summary of the results and their implications.

3.2. Available data from SAXS microscopy. An overview of the information content obtained from a measurement is shown in Figure 3. On the left we show a microscopic image of a thin section of Opalinus Clay, cut parallel to bedding. The area indicated by the red dotted lines was scanned, and the images in Figure 3(a)−(e) represent integrated SAXS maps showing different properties. Each pixel in each map represents a single measurement assessing a volume of approximately 25 × 10 × 30 μm^3 over the entire scanning area of 1.50 × 2.75 mm^2. For every measurement an orientation analysis using eq 5 was performed. That way, for each scanning volume, the parameters a_0 (average intensity), a_1 (oriented intensity), and α_s (orientation angle of the scattering pattern) were extracted. In Figure 1 it is shown how the parameters are related to the intensity distribution represented by the scattering pattern. For each map the pores have a diameter $d \approx \frac{2\pi}{q} \approx$ 20−30 nm. In principle any other pore-size range can be selected and visualized from 4 to 130 nm. The maps in Figure 3 illustrate (a) the total absorption (X-ray microscopy), (b) the degree of orientation a_1/a_0, (c) the orientation of the scattering pattern α_s, (d) the intensity exponent, and finally (e) the asymmetric and symmetric intensity together with the orientation of the scattering pattern, a_0, a_1, and α_s, respectively.

The absorption map in Figure 3(a) is an X-ray microscopic measurement where dark pixels correspond to high-absorbing (dense) phases. The map is a first indication of mineralogy and makes the interpretation of the scattering pattern much easier. It shows microscopic minerals or fossils that can be approximately 10−100 μm in diameter, surrounded by a rock matrix that cannot be resolved further. A distinct large grain of several hundred micrometers is situated in the center of the sample. That implies that the spot size of the measurement resolves rock matrix and microscopic mineral grains or fossils.

In Figure 3(b) the local degree of orientation is shown. This parameter has values from 0 to 1, representing pores of low random orientation or a very high degree of orientation of preferentially aligned pores, respectively. The local degree of orientation can be as high as 0.25, meaning that pores can be moderately oriented. Overall, the orientation does not appear to follow a distinct systematic pattern, although some high values occur around some of the larger grains in the center of the pattern.

The main orientation of the scattering pattern α_s is displayed in Figure 3(c), which is always perpendicular to the orientation angle of the scattering pattern. For example, if a pixel suggests an average orientation of the scattering pattern at 90°, pores in that volume are facing toward 0°. So with this map the local orientation of pores can be visualized. It can be seen that the orientation distribution does not follow a specific pattern.

The intensity exponent in Figure 3(d) shows the decay of the scattering intensity $I(q)$ on a log/log scale. The curve typically follows a power-law whose exponent m is defined as $I(q) \approx q^{-m}$. The map shows the value of m for the given q range. The exponent quantifies the fractal nature of scatterers, for most shales indicating either a surface or a mass fractal,[30] or may be interpreted as a power law pore-size distribution.[52] In map (d) it is shown that the intensity exponent varies locally from about 3.01 to 3.24, although again not following a specific pattern.

Figure 3(e) shows three combined parameters: the orientation, and the isotropic as well as anisotropic scattering intensities. As in map (c), the color-coding represents the

DOI: 10.1021/acs.energyfuels.6b02256
Energy Fuels XXXX, XXX, XXX−XXX

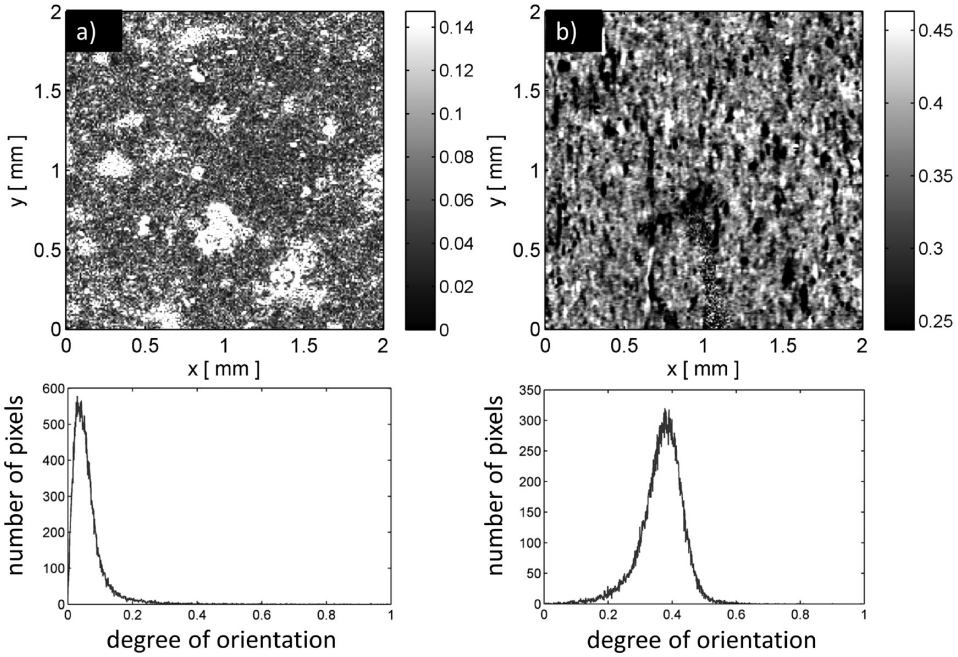

Figure 5. Degree of orientation and average orientation for Jordan shale samples cut parallel (a) and perpendicular (b) to bedding. The variation in orientation associated with microfossils and voids. The average degree of orientation is higher for the rock cut perpendicular to bedding. The graphs show the number of pixels having different degrees of orientation. For the rock perpendicular to bedding, the average orientation is approximately 0.4, while, for the rock cut parallel, it is less than 0.1.

average orientation of the scattering pattern, as indicated in the color wheel. The brightness of a pixel indicates the scattering intensity. If the color is white, there is isotropic scattering; hence, the volume contains randomly oriented pores. If the pixel is colored, then oriented pores are present, and a bright color in both cases indicates a higher scattering intensity. So the map shows the relative abundance of pores—which is related to the scattering intensity—together with the average orientation of pores. As in Figure 3(c), the orientation in Figure 3(e) appears to be more or less random. A slight trend toward a preferential orientation of the scattering pattern to 30°−50° (green color code) might be interpreted. The reason for that could be that the thin section, even though prepared parallel to bedding, was accidentally cut at a low angle, causing a slight anisotropy of the scattering pattern. The observation could also explain why the orientation values are larger than expected for measurements performed perpendicular to sample bedding.[17] Figure 3(e) suggests that the large mineral grain has a lower scattering intensity than surrounding scanning volumes, suggesting that it is less porous. In the vicinity of the grain, pores seem to be more abundant with preferential alignment and a distinct orientation.

The maps shown in Figure 3(a)−(e) provides a quick overview of the pore orientation over the entire scanning area covering several square millimeters. At the same time, the method is able to resolve local differences in the degree of orientation, orientation angle, scattering intensity, and intensity exponent. These details would be averaged out in a SANS measurement where a much larger spot size of several square centimeters is employed. Because of the high scanning resolution (25 × 10 × 30 μm^3 per pixel over 40,000 pixel), sample sizes can be investigated that are on a scale comparable to μ-CT and BIB-SEM images.

3.3. Pore orientation. The orientation analysis over different sample volumes reveals detailed aspects of the local structural alignment of pores. We apply the same orientation analysis scheme as shown in the previous section, but on different rocks. Here we focus on the local pore alignment and pore orientation as a function of rock type and rock orientation. Figure 4 shows the results for the France shale sample cut perpendicular to bedding. A preferential orientation and high degree of orientation are expected due to its deep burial. Figure 4(a) shows the degree of orientation, and (b) shows the pore orientation together with isotropic and anisotropic scattering intensity for pores from approximately (20−30) nm in diameter. The average degree of orientation is high, mainly between 0.9 and 1, suggesting that the pores have a strong preferential orientation. It varies locally, and a lower degree of orientation is connected to isolated elongated spherical areas several micrometers long. A low degree of orientation can also be connected to even larger microscopic features. An example for this is located at a distance of approximately 0.7 mm on the x-axis. At this location the scanning area is intersected by a black band approximately 50−100 μm wide, with a degree of orientation below 0.9. Figure 4(b) suggests that the average orientation of the scattering patterns is horizontal (cyan on the color wheel); hence, the pores are oriented in a vertical direction, which is the direction of the bedding plane (marked with the red arrow and parallel lines). However, the results show that both parameters vary locally. The areas of low degree of orientation, in contrast, do not show a preferential orientation, and they have a low scattering intensity, i.e. contain relatively fewer pores.

It can be concluded that the degree of orientation, orientation, and anisotropic and isotropic scattering intensities vary locally. Here low values of both scattering intensity and degree of orientation are connected to large features. The shape and distribution of these objects suggest that they represent larger grains within the clay matrix. These are expected to be less porous, and without any preferential orientation. There-

DOI: 10.1021/acs.energyfuels.6b02256
Energy Fuels XXXX, XXX, XXX−XXX

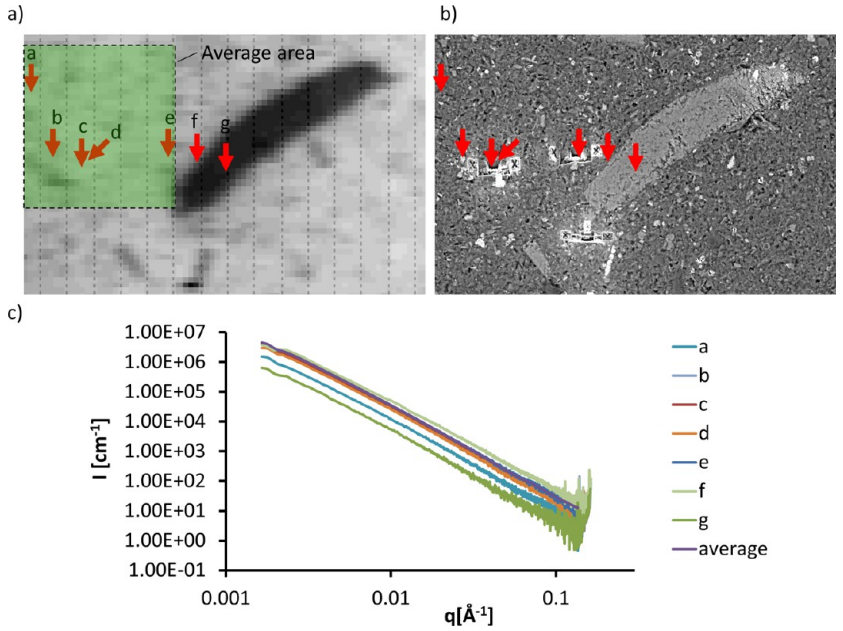

Figure 6. Individual scattering volumes, red arrows (a–g), were selected on the basis of SEM images (b) and the absorption map (a). An average curve from all the scattering volumes is created to compare scattering intensities I(q) for each volume (c). The average area that overlaps with the SEM field of view is shown in green. The corresponding $I(q)$ show a maximum relative shift of an order of magnitude in intensity on the vertical axis.

fore, the elongated feature most likely represents either a crack or a mineral vein. Compared to the results shown in Section 3.2, where the pore orientation is random, we identify a clear preferential orientation of pores subparallel to bedding in this case. This was also observed and suggested by results of SANS studies on shales by Gu et al.[17] The average degree of orientation is generally much higher than shown in Figure 3. This outcome is expected to be due to the preferential orientation of pores subparallel to bedding.

In Figure 5 the degree of orientation of pores varying in size from 20 to 30 nm is shown for the Jordan shale. The analysis is performed on two twin samples cut parallel (Figure 5(a)) and perpendicular (Figure 5(b)) to bedding. The degree of orientation varies locally but irrespective of rock orientation. In the present example, matrix properties vary at the micrometer scale. The average degree of orientation is approximately 0.4 in (a), whereas it is <0.1 for (b).

The rock contains perforated and hollow foraminifera shells that show a strong degree of orientation connected to the shell wall. Elongated voids within the shells show no orientation. The results show that the overall degree of orientation is higher for the rock cut perpendicular to bedding. Compared to the France shale, the Jordan shale cut perpendicular to bedding shows a lower overall degree of orientation, which is connected to the geologic history of the rock. The oil shale experienced less burial compared to the (low metamorphic) France shale sample.

For all rock types shown, including Opalinus (Figure 3), France (Figure 4), and Jordan shale (Figure 5), the local variation of the degree of orientation and orientation was determined successfully. In all cases, this variation was related to mineral grains or fossils. The strong contrast in scattering behavior can only be resolved because of the small spot size used. Only an average value would be obtained in a typical SANS experiment—using a larger beam—covering an area of several square millimeters. The data here suggest that such an averaged parameter for the degree of orientation could overestimate or underestimate the local degree of orientation. A contrast of those properties could also have an effect on the effective volumetric or flow properties of the rock, such as where volumes with lower degree of orientation might represent flow-barriers.

3.4. Porosity and pore volume distribution. SAXS allows the determination of porosity and pore-size distribution, which in relation to gas shales provides information on gas-in-place as well as first indications of transport properties. The results in Sections 3.2 and 3.3 suggest a local contrast in scattering intensity, indicating a relative contrast in porosity. While we expect large contrasts for these parameters between matrix and microscopic grains, we also want to examine the variation of matrix porosity. The rock investigated is Opalinus Clay cut parallel to bedding. The assessment is on a pixel-by-pixel basis. The pixel selection was done on the absorption map in Figure 6 supported by an SEM image taken after the SAXS experiment (Figure 6, right). The SEM image represents a high-resolution image of the surface mineralogy of the thin section used in the SAXS experiment, including the scanning area. Initially both images were registered onto each other as described in Section 3.6, such that SAXS volumes could be selected according to surface mineralogy in the SEM image. Here in the first part we quantify the local variation of porosity calculated from the SAXS scattering curves. Then we will compare the results for the calculated pore-size distributions from each individual volume to complementary SANS and N_2 sorption data.

All positions of the selected volumes are shown in Figure 6 (red arrows a–g) on the absorption map (Figure 6(a)) and the respective SEM image (Figure 6(b)). Each volume was selected on the basis of the SEM image intended to target rock matrix (red arrows a–e), the contact zone mineral grain and matrix (arrow f), and a calcite mineral grain (arrow g). The corresponding $I(q)$ values are shown in Figure 6(c) and are compared to an average scattering curve for the sample. The average scattering curve is obtained from 1280 individual

DOI: 10.1021/acs.energyfuels.6b02256
Energy Fuels XXXX, XXX, XXX–XXX

scattering volumes, covering a sample area of approximately 400 × 400 μm^2. The part that overlaps with the SEM field of view (more than 70% of the area is overlapping) is shown in the absorption map of Figure 6. The total variation observed ranges over about an order of magnitude in intensity. Except for the curve representing volume (a), all curves intended to target the rock matrix (a)−(e) are not shifted more than a factor of 2 from the average curve on the horizontal axis. Volume (g) has the lowest and (f) the highest intensity.

The porosities calculated from the $I(q)$ curves of each volume (Table 3) suggest that porosity varies locally. Porosity represents the total pore volume (connected and unconnected) of all pores of radius 1.5−125.9 nm. The observed porosity range is from 2.1% to 23.8%. The lowest porosity of 2.1% relates to the calcite grain. It is considerably lower than the average of 14.8%. The lowest porosity for volumes in the rock matrix is 5% and assigned to location (a) in Figure 6. This is approximately one-third of the average porosity. The second lowest is attributed to location (c) and is 3.8% less than the average. The highest porosity of 23.8% was measured for location (f), just next to the calcite grain in location (g). The remaining locations in Figure 6(b)−(e) show a small but measurable porosity variation relative to the average value, with porosity values roughly between 11% and 15%. For comparison, the average porosity for the SAXS data is 1.9% lower than the measured SANS porosity of 16.6%. The reason could be that the average porosity of the two studied samples was different.

Table 3. Calculated Porosities of the Different Targeted Volumes in the Rock Matrix and Mineral Grains

sample	targeted area	porosity [%]
a	matrix	5.0 ± 0.5
b	matrix	13.7 ± 1.4
c	matrix	11 ± 1.1
d	matrix	12.3 ± 1.2
e	matrix	15.5 ± 1.6
f	contact matrix/calcite grain	23.8 ± 2.4
g	calcite grain	2.1 ± 0.21
average	average	14.8 ± 1.5
SANS	average	16.6 ± 1.7

Not surprisingly, a large difference between grains and matrix porosity can be observed. An unexpected outcome, however, is the large difference in matrix porosities of 10.5% ((a)−(e)). Busch et al.[26] investigated up to 13 Opalinus Clay samples from one core section and found a narrow porosity range. Further, previous studies suggest that the sample volumes studied here are well within the expected representative elementary volume (REV) for the rock matrix in Opalinus Clay. For instance, Keller et al.[20] found that a FIB-SEM measurements volume of 10 × 10 × 8 μm^3 for Opalinus Clay was close to an REV for the rock matrix: This is much smaller than the sampling volume of 25 × 10 × 30 μm^3 used here. A possible reason for the variation is that the volumes targeted by the SAXS not only contain rock matrix, but also microscopic grains, that have considerably lower porosity, thus lowering the effective measured porosity. Evidence for large grains differing in length in our data can be found in the absorption map in Figure 3 (large mineral grain in the center).

Another reason for the variation of measured porosity values could result from errors in the SLD calculation related to mineralogical heterogeneity. As small volumes are targeted, the mineralogical composition is expected to vary significantly. Mineralogical heterogeneity would lead to variations of the true average scattering length density affecting the calculation of porosity. A strong effect is expected from the presence of pyrite or siderite in the volumes. However, as shown in Table 2, pyrite and siderite only contribute 1% and 0.8% to the bulk mineralogy, respectively; hence, for this example no strong effect is expected. Only for rocks that have high (local) concentrations of high-density minerals might this effect become relevant.

The pore-size distributions may help to understand the differences observed in average porosities between SAXS and SANS measurements and between individual volumes. In the following, the pore-size distribution of the average SAXS curve is compared to the pore-size distributions of SANS, and additionally to N_2 adsorption data, to benchmark the SAXS results against multiple methods. We assume that similar structures have a similar pore-size distribution. Then we also

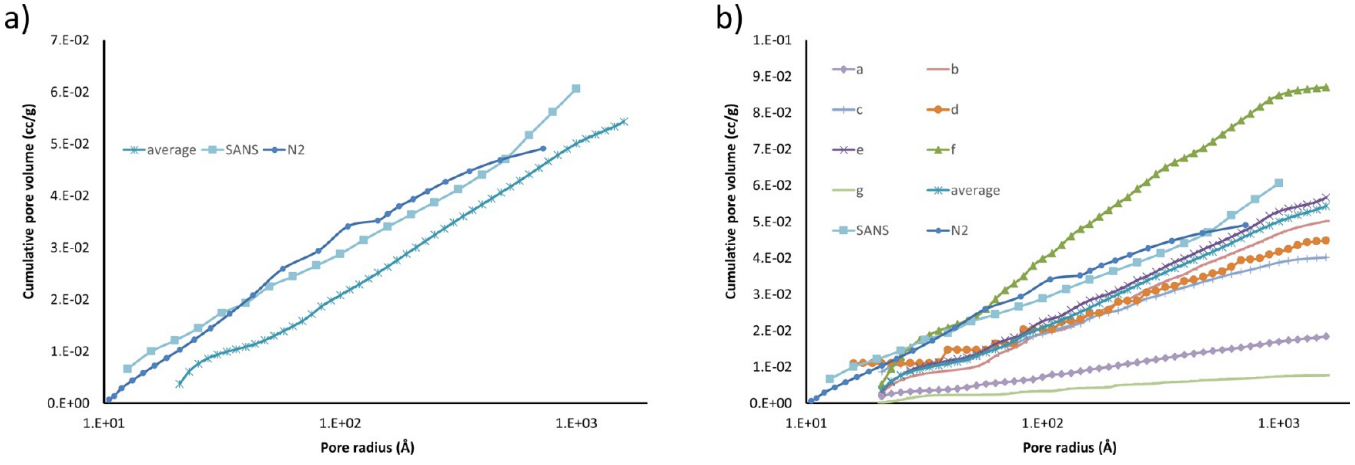

Figure 7. Pore volume versus radius distribution of the SAXS data compared to SANS and N_2 adsorption measurements. Volumes (c), (b), and (e) generally fit well to the average curve, indicating that the pore system is similar. Curves (a), (f), and (g) show strong variation related to differences in the pore structure. Volume (d) seems to have a similar pore structure compared to volumes (b), (c), and (e), though at lower magnitude. The results also show that volumetric properties can deviate substantially from the average curves.

DOI: 10.1021/acs.energyfuels.6b02256
Energy Fuels XXXX, XXX, XXX−XXX

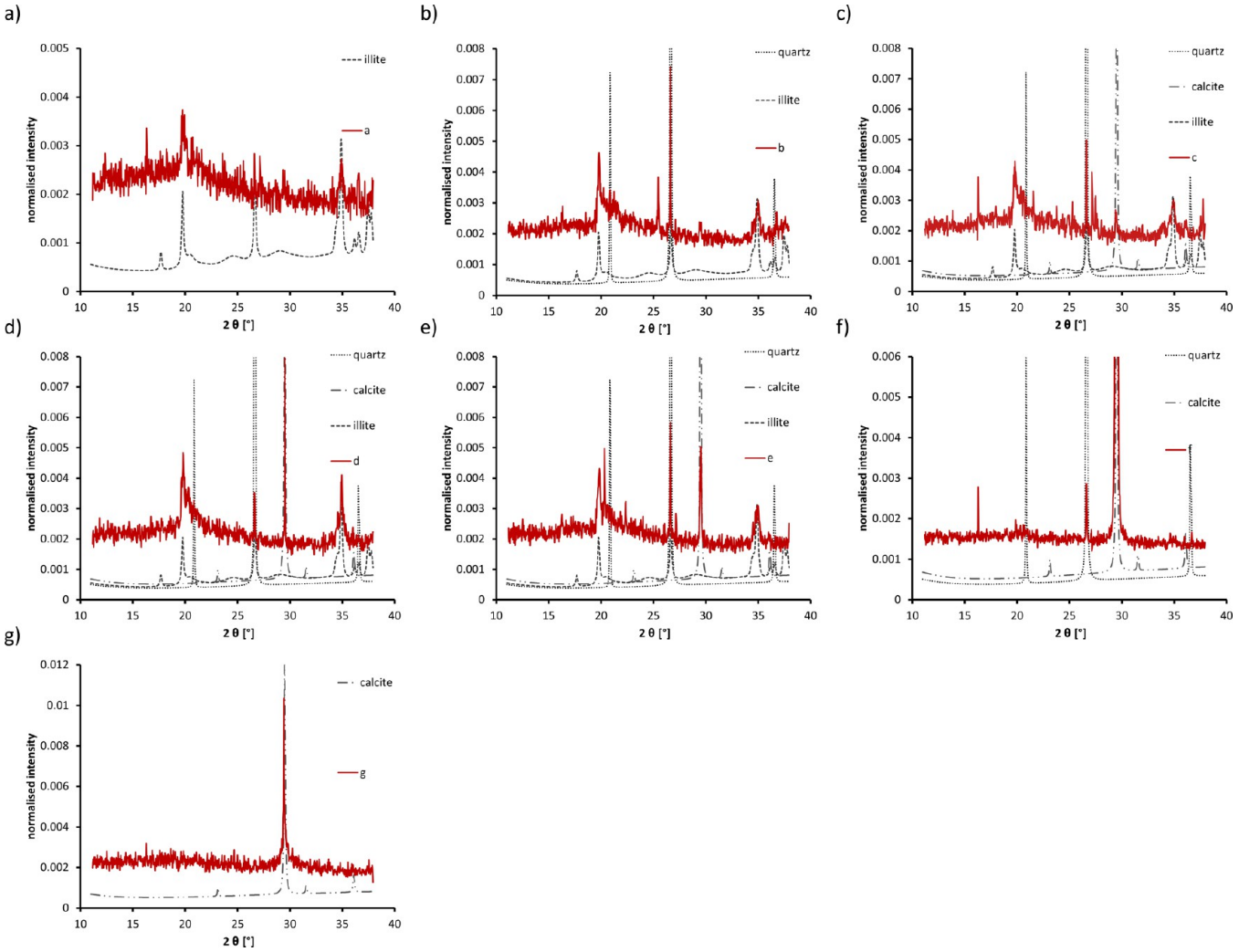

Figure 8. WAXS patterns from the volumes (a)−(g) are compared (red) to the scattering pattern (gray and black) for single minerals. In volumes (a)−(e), Illite is present. Volumes (f) and (g) differ in mineralogy, only containing calcite (f and g) and quartz (f) but no clay minerals.

compare the individual pore-size distribution of volumes (a)−(g) to the average SAXS results. Calculated pore volume distributions versus the pore radius of all the subvolumes studied, including the average curve, SANS, and N_2 adsorption, are shown in Figure 7.

The agreement between N_2 adsorption SANS and the average SAXS curve shown in Figure 7(a) is satisfying and documents that all methods determine a similar pore space. Volumes (b) and (e) shown in Figure 7(b) fit well to the average curve, only showing minor variations relative to each other. Volumes (c) and (d) fit reasonably well to (average, b, e) but have less macropore volume. Volumes (a, f, g) represent a different pore structure compared to the average curve because they have strongly differing slopes.

The first observation is that the pore-size distributions of the rock matrix and mineral grains are different, which is in line with the correspondingly low porosity. Another observation is that local variation is measurable between volumes (a)−(e), that are most likely targeting matrix volumes. As discussed, a reason could be the presence of large nonporous grains in the scattering volume reducing the effective porosity and decreasing the intensity magnitude. Overall, it is difficult to make a clear statement on what causes the variation.

We conclude that one way to individually investigate local effects is to quantify phase-specific properties by reducing the scattering volume size. This could be achieved by reducing the beam size, the sample thickness, or a combination of both. This would allow detailed studies of the microstructure, determining the role of components in the pore network by statistically studying the volumetric properties and the microstructure. A possible application could be to quantify pores in the rock matrix, organic matter-rich volumes, or volumes connected to clay minerals. The results have shown that decreasing the beam size of a SAXS measurement applied to shales also means that it may become increasingly important to know what mineral phases are present in the scattering volume, for an accurate SLD calculation or to understand the observed variation in properties.

3.5. WAXS and mineralogy. The surface mineralogy of the area targeted by a small-angle scattering beam does not necessarily represent the average composition of the scattering volume, if the volume size is small. Additional information about the mineralogy of the scattering volume may be required to understand local differences in porosity and pore-size distribution.

We have combined WAXS and SAXS from identical volumes. Here we determine minerals present in the scattering volume of

DOI: 10.1021/acs.energyfuels.6b02256
Energy Fuels XXXX, XXX, XXX−XXX

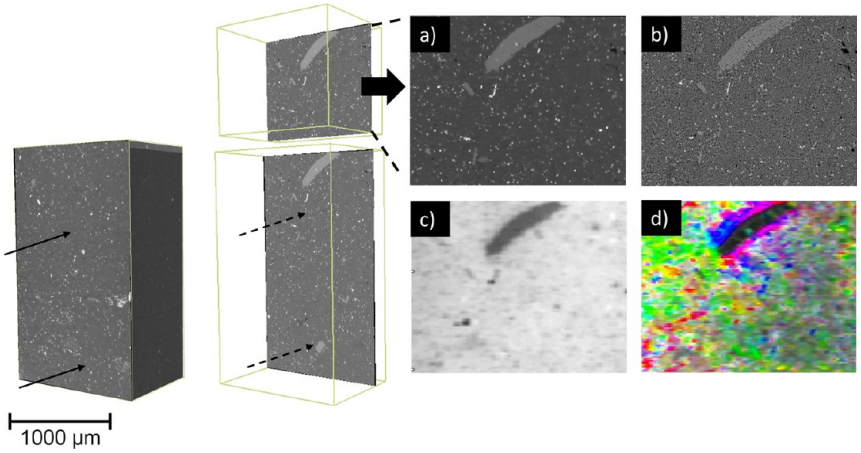

Figure 9. Visualization of the image registration for Opalinus Clay. The μ-CT scan shows a 1 μm^3 voxel resolution 3D map of the electron density distribution of a volume of Opalinus Clay (a). After preparing a thin section from the sample, SEM images with submicron resolution were one-to-one registered into the 3D volume (b). The absorption map (c) with a pixel size of 10 × 10 μm^2 is used to 3D register the SAXS data (here showing the orientation and scattering intensity map (d)) to the 3D volume.

the selected regions (a)−(g) shown in Figure 6. Mineral identification is performed by peak fitting of the WAXS data. In general, each mineral shows a unique combination of high-intensity peaks at a given 2θ corresponding to its crystal structure. A mineral phase can then be identified from a WAXS pattern, if the peaks observed are at the same position as in the expected scattering behavior for the mineral. This requires knowledge of the scattering behavior of the minerals present as well as of the mineralogical sample composition. Here the reference is a Rietvelt refined XRD pattern of a twin sample of the same mineralogy.[26] The refined data also shows the corresponding scattering pattern of the individual minerals that contribute to the total scattering pattern. The mineralogy is presented in Table 2; we selected the key minerals from Table 2 and compare the simulated pattern for individual minerals to the WAXS data of volumes (a)−(g).

In Figure 8 the intensities of the experimental data are shown in red and the expected patterns for the different minerals are marked in gray−black lines, for the volumes (a)−(g). The intensities shown are normalized to the total intensity, to better compare expected and experimental data. The results suggest that all volumes (a)−(e) contain Illite. In addition, volume (b) contains quartz, while (c)−(e) contain calcite. The other two volumes seem not to contain Illite, while (g) only contains calcite. While the XRD data of the sample suggest more than 21% of kaolinite, the signal was not present in the WAXS pattern of the tested volumes. In addition, the pattern also showed additional peaks which were not identified. One example is volume (c), with two nonidentified peaks at 27.13 and 27.43°. Those two peaks would match the pattern of K-feldspar; however, the experimental pattern is also missing many of the peaks that are expected for K-feldspar at lower angles.

The measurements confirm that all volumes (a)−(e) targeting the rock matrix contain Illite, the main constituent of the matrix. Volumes (f) and (g) differ in mineralogy; (g) only contains calcite, while neither sample contains clay.

Identifying the minerals in the pattern alone, however, could not explain the differences in porosity that were observed in section 3.4. Rietvelt refinement of the pattern could resolve the mineral quantity.[16,40] This could help to connect mineralogy to porosity. It was not attempted here because the detector used in the experiment covered a very limited angular range, as shown in Figure 1. Because of preferential mineral orientation and detector size, our analysis most likely does not capture all the minerals present. This is also the likely reason that not all the peaks in the pattern could be identified in volume (c). Some reflections were either not produced because of the mineral orientation or not captured by the detector.

Several studies have shown that the preferred mineral orientation can also be quantified from texture analysis of a full detector WAXS pattern.[16,40] Mineral orientation certainly influences rock mechanical and flow properties.[16,40] We therefore suggest the combination of mineral orientation porosity and pore-size distribution as well as pore orientation derived from SAXS analysis in future research. We propose to perform both full detector scanning SAXS-WAXS experiments, in combination with SAXS and statistical analysis of the data.

3.6. Image registration. In this section we combine μ-CT, SEM, and FIB-SEM imaging with SAXS and WAXS microscopy. Figure 9 shows that scanning SAXS-WAXS microscopy can be integrated into a multiscale imaging workflow. SEM imaging yields tens of nanometers to submicrometer information about porosity and surface mineralogy (Figure 9(b)), although only in 2D. The SEM image is used for registering into the 3D μ-CT scan volume in Figure 9(a). In this example a large calcite grain in the center in Figure 9(b) makes the registration process much easier. Since the feature extends over hundreds of micrometers, it can be easily recognized in all the data. For example, it can be easily resolved in the X-ray absorption map, Figure 9(c), extending over the entire SAXS scanning area. This map is first used for image registration in relation to Figure 9(a) and Figure 9(b). Once the registration of the absorption map is completed, the coordinates obtained from the image registration can be applied to all other SAXS data (Figure 9(d)). As a result, μ-CT and SEM data can be directly compared and combined with all types of SAXS/WAXS data, as shown in sections 3.2−3.5.

The absorption map is suitable for image registration because it shows the density distribution and resolves similar features as the μ-CT scan. However, the success crucially depends on the dimensions of the SAXS beam. The current beam size for scanning SAXS-WAXS is 10 × 25 μm^2, which is approximately a factor of 250 higher than the μ-CT voxel resolution. Smaller

DOI: 10.1021/acs.energyfuels.6b02256
Energy Fuels XXXX, XXX, XXX−XXX

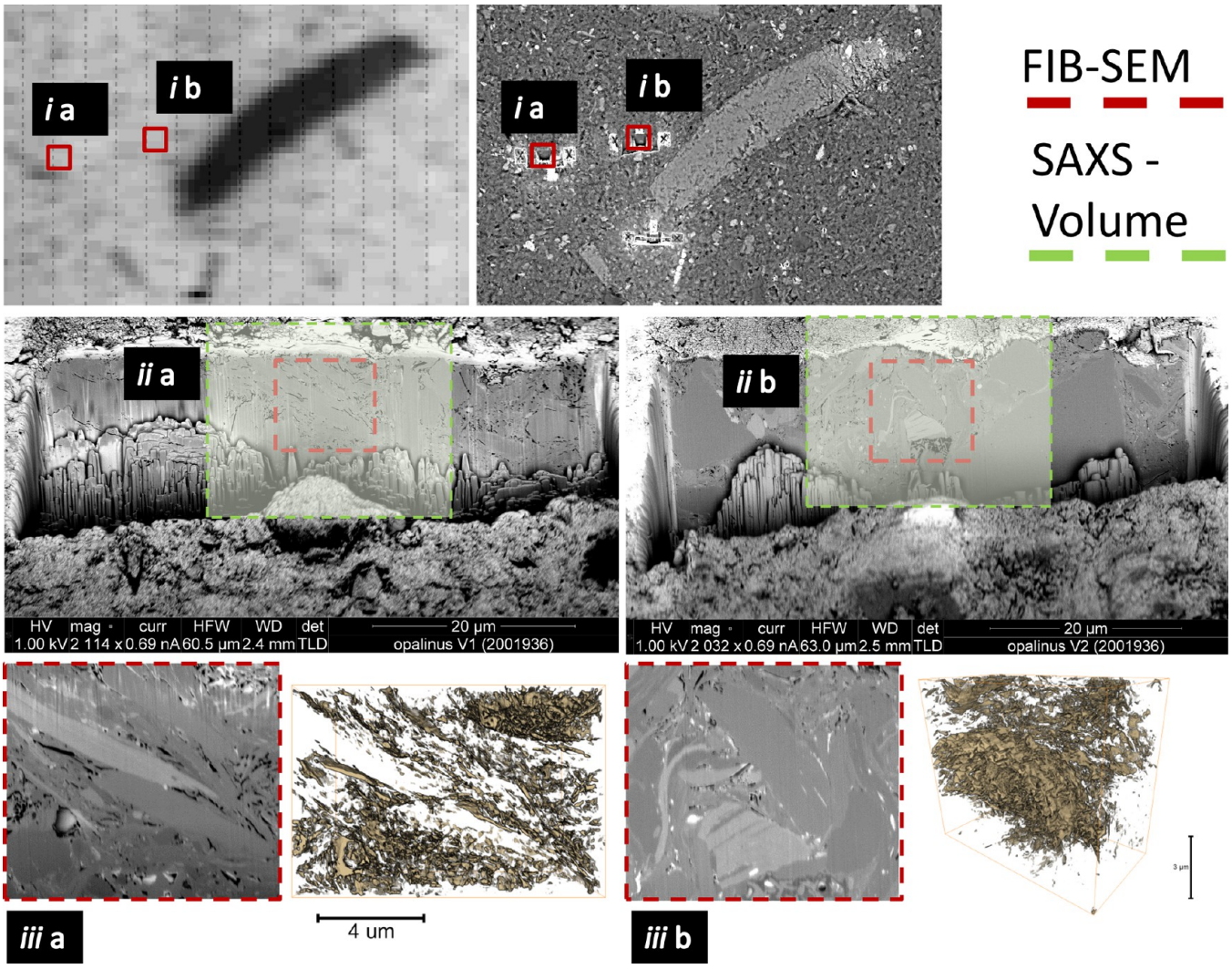

Figure 10. After FIB-SEM imaging, the volumes which were milled out with the FIB can be 1 to 1 relocated in the SEM (*i*a and *i*b). Hence the SEM is registered to the μ-CT and scattering data the scattering information can be extracted for the individual volumes (*i*a and *i*b). This allows direct comparison of the FIB-SEM data and scattering data. Due to the beam size, the effective volume targeted by the SAXS (green box *ii*a and *ii*b) is still larger than the FIB-volume (red box *ii*a and *ii*b). The segmented FIB-SEM data can be used to visualize pore orientation and calculate volumetric properties (*iii*a and *iii*b).

submicron features such as shells or pyrites could remain unresolved and, thus, may be represented as a "mixed" SAXS signal.

After the SAXS data was acquired, FIB-SEM imaging was performed on two spots, targeting the rock matrix, to obtain high-resolution 3D images. For that, two trenches measuring approximately 80 × 40 × 20 μm^2 were FIB milled on the sample. The cuts were perpendicular to the surface of the thin section and perpendicular to the bedding plane. Then the FIB-SEM volumes were selected on the basis of the trench, and two FIB-SEM volumes of the microstructure were milled and imaged. After the FIB-SEM imaging, we captured another post-SEM image of the sample surface. Once the SAXS and WAXS data are registered to the SEM and μ-CT data, FIB-SEM data can be located on the SAXS data as shown Figure 10. The ion milling trenches with a depth and width of several micrometers can easily be spotted in the postmilling SEM image of the scene, as indicated in the red boxes in the upper right of the image Figure 10 (*i*a and *i*b). With the help of the overview SEM, the scattering data for the FIB-SEM volumes can be superimposed (Figure 10 upper left image *i*a and *i*b). The width and depth and length extent of the SAXS volume exceed the FIB-SEM volume, as shown in Figure 10 (*ii*a and *ii*b). The segmented FIB-SEM data give detailed information on the size and distribution of the macropores as shown in Figure 10 (*iii*a and *iii*b).

In FIB-SEM studies, a pore is normally only resolved if it spans at least 3 voxels, which means that pores of diameter <20 nm cannot be represented correctly for typical FIB-SEM with a voxel size of 5−10 nm.[20] In this study the voxel size is 10 nm. This resolution gap results in an unconnected pore space for many rock samples.[20] A successful registration of SAXS and FIB-SEM data means that the lower part of the mesopores can be measured for a rock volume targeted by FIB-SEM.

Repeatable measurements from different experimental techniques are required for systematic studies of the shale microstructure. However, it has been shown that different experimental techniques, especially small-angle scattering and imaging techniques, produce systematically different results for porosity.[26] Therefore, for better understanding of the

DOI: 10.1021/acs.energyfuels.6b02256
Energy Fuels XXXX, XXX, XXX−XXX

uncertainties and limitations of experimental methods we use to characterize pores in shales, direct comparisons are needed. This, however, is often difficult because either physically different samples have to be used or incomparable volume sizes of several orders of magnitude difference are assessed by different experimental techniques, possibly introducing an error due to sample heterogeneity.

Here we show the application of SAXS and imaging on a largely overlapping sample volume, where the volume targeted by SAXS is only approximately a factor of 12 larger than the FIB-SEM volume. This difference, however, could be minimized in future experiments through reducing the sample thickness and SAXS spot size. It would allow direct comparison of both techniques to benchmark results of the experiments.

3.7. Summary and implications on SAXS-WAXS analysis on shales. We have explored scanning SAXS−WAXS microscopy as a rock characterization tool. The motivation is to overcome the limitations of scattering and imaging or shale characterization by combining their individual advantages. X-ray scattering with a small spot size enables the local assessment of pore orientation and volumetric properties. It allows pore-size distributions to be inferred, with a quantification of size for even the smallest (nanometer-sized) pores in shales that may not be captured by even the highest-resolution imaging techniques. Because of the high scanning resolution determined by the small spot size, the results can be registered directly to 3D images, which provide a more complete representation of the pore space at larger scales, above 100 nm.

The results demonstrate that a crucial part for the success of this effort is the beam spot size and sample thickness. The spot size in this experiment was small enough to measure the local variation of orientation and volumetric properties. The orientation, degree of orientation, porosity, and pore-size distribution vary locally. Strong differences in orientation and volumetric properties may act as flow-barriers that influence the macroscopic flow properties over several millimeters. Strong variations from the average rock matrix behavior could be attributed to mineral grains, and fossils that range from sub-micrometers to several micrometers in size. It was also found that a smaller local variation, primarily of the volumetric properties, was apparent within the rock matrix.

We propose two ways to improve the quantification of the variation caused by structural differences related to material properties of different phases, from effects induced by local mineralogical heterogeneity. In the ideal case, both the beam size and sample thickness need to be further reduced. The aim here is to reduce the scattering volume size to target individual components of the structural local heterogeneity within the rock matrix. The underlying idea is that the smaller the volume, the fewer phases are present, allowing the accurate resolution of individual components. Statistical analysis of the data that is collected over a large scanning area will lead to a clearer picture of the roles of components in the matrix. When reducing the spot size and sample thickness, a smaller volume is targeted. Both mechanisms increase the scanning time significantly. So, most likely, there is a practical limit, which means there will always be some heterogeneity left in the scanned volume. A way to deal with this heterogeneity might be a comprehensive statistical analysis of the data. This is also one of the strengths of scanning SAXS and WAXS microscopy, where, in a short time, a large amount of data is collected. Therefore, by measuring multiple volumes over a large area of the rock, a large heterogeneity and associated variation of the microstructure can be assessed. A possible application of the method could then be using organic-rich shales to measure differences in organic matter: pyrite and clay mineral porosity and pore-size distributions. The method could also be applied for REV analyses in shales or other heterogeneous porous materials. This can be established by investigating the number of scanning volumes required to reach a constant porosity and/or mineralogy. As shown in Figure 3, the five scanning areas covered reach at least several square millimeters, which can effortlessly be further increased (at the cost of measurement time, and limited by sample size) to capture an REV. Systematic studies of the variation will lead to a better characterization and understanding of the shale pore network and the scales over which it varies.

A further reduction of the spot size, however, makes it increasingly important to know the mineral phases present in the volume investigated. When reducing the spot size, the mineralogical heterogeneity increases. Minerals in the scattering volume determine the SLD and thus affect the calculated porosity. So reducing the spot size makes the interpretation of measurement more complex, because every scanned volume can have a different mineralogy. The reduction, however, also gives the opportunity to make the measurement more accurate, if the mineralogy is known.

While WAXS measurements in this study gave valuable insight into the minerals present in the volumes investigated, the detector was too small to capture the reflections at all angles. Thus, full detector measurements are needed to capture all mineral reflections. Even though a quantitative mineralogy will be biased by preferential orientation of minerals, it might be necessary to attempt mineral quantification for a more accurate SLD calculation. Full detector WAXS would add valuable information on the preferential orientation of mineral components that also determine porosity, connectivity, and mechanical properties. We therefore think that in future experiments SAXS and full detector WAXS should be combined.

SEM, FIB-SEM imaging, and small-angle scattering data can be directly combined and registered to each other. This combination allows direct comparison of volume-averaged pore-size distributions and porosity distributions of both methods. As a result, the effective measurable pore-size range of BIB-SEM and FIB-SEM can be enhanced, including pores of radius as small as 1.5 nm. It is crucial to understand orientation, porosity, and pore-size distribution in the mineralogical context and the distribution of the pores on all relevant scales for establishing meaningful predictive models for flow, transport, and storage processes. We think that scanning SAXS-WAXS microscopy has a large potential to address these points.

4. CONCLUSIONS

In this study we have applied scanning SAXS-WAXS microscopy to better understand porosity, pore-size distribution, and pore orientation in shales. The novelty over common application of small-angle scattering techniques on shales is that local but volume-averaged information is obtained. This is achieved by operating the method in a scanning microscopy mode where the beam is focused to microscopic scanning volumes. This application makes it possible to target microscopic volumes and at the same time collect statistically relevant data for large sample volumes. We show that, combined with

DOI: 10.1021/acs.energyfuels.6b02256
Energy Fuels XXXX, XXX, XXX−XXX

WAXS, local porosity, pore-size distribution, pore orientation, and mineralogy can be locally resolved in one measurement.

We have demonstrated that this method can be combined with μ-CT, SEM, and FIB-SEM imaging on the same sample volume, extending the measurable range of imaging methods down to pore sizes as small as 3 nm. The method thus allows the systematic analysis of the distribution of the smallest pores connecting larger pores that are crucial for gas storage processes. For meaningful predictive models, it is crucial to represent this pore class accurately.

The local porosity and pore-size distribution of pores ranging from 1.5 to 150 nm in Opalinus Clay strongly vary over micrometer scales. However, we found that the spot and sample thickness were too large to further resolve and fully explain these variations. For future applications, we suggest reducing the spot size and sample thickness even further. The measurements may then be used to directly measure pore-size distributions and porosity of organic matter, matrix, and other rock components. This would improve the understanding of the distribution and role of mesopores for transport and storage processes in the shale pore network.

The combination SAXS and later FIB-SEM on nearly the same sample volume allow direct comparison of both techniques. This application may improve assessing errors and uncertainties of small-angle scattering and FIB-SEM imaging to characterize the shale pore system.

Future application of SAXS and WAXS could be used to link pore orientation, pore volume, and mineral orientation for systematic studies on flow and mechanical properties of the microstructure. Thus, it could be used to determine REVs for porosity and mineralogy in shales and other heterogeneous porous media.

AUTHOR INFORMATION

Corresponding Author

*E-mail: l.leu14@imperial.ac.uk.

Notes

The authors declare no competing financial interest.

ACKNOWLEDGMENTS

We would like to express our gratitude to Johannes Klaver for providing samples from his Ph.D. project and Swisstopo for making Opalinus Clay samples available. Ab Coorn is greatly acknowledged for his sample trimming skills. Fons Marcelis is thanked for performing SEM/EDX measurements as well as providing sample material and establishing contacts with external companies. Sander Huisman and Sergio Fernandez from Panterra B.V. are thanked for dedicated sample preparation. Henning Peters is thanked for helpful discussions. We would like to thank Joachim Kohlbrecher for discussions on data interpretation. This project was supported with funding from Shell Global Solutions International B.V.

REFERENCES

(1) Clarkson, C. R.; Jensen, J. L.; Chipperfield, S. (2012) Unconventional gas reservoir evaluation: What do we have to consider? *J. Nat. Gas Sci. Eng.* **2012**, *8* (0), 9−33.

(2) Blunt, M. J. Flow in porous media — pore-network models and multiphase flow, Current Opinion. *Curr. Opin. Colloid Interface Sci.* **2001**, *6* (3), 197−207.

(3) Clarkson, C. R.; Solano, N.; Bustin, R. M.; Bustin, A. M. M.; Chalmers, G. R. L.; He, L.; Melnichenko, Y. B.; Radlinski, A. P.; Blach, T. P. Pore structure characterization of North American shale gas reservoirs using USANS/SANS, gas adsorption, and mercury intrusion. *Fuel* **2013**, *103* (0), 606−616.

(4) Sing, K. S. W. Reporting physisorption data for gas/solid systems; with special reference to the determination of surface area and porosity. *Pure Appl. Chem.* **1982**, *54* (11), 2201−2218.

(5) Loucks, R. G.; Reed, R. M.; Ruppel, S. C.; Hammes, U. Spectrum of pore types and networks in mudrocks and a descriptive classification for matrix-related mudrock pores. *AAPG Bull.* **2012**, *96* (6), 1071−1098.

(6) Desbois, G.; Urai, J. L.; Kukla, P. A. Morphology of the pore space in claystones—evidence from BIB/FIB ion beam sectioning and cryo-SEM observations. *eEarth* **2009**, *4* (1), 15−22.

(7) Klaver, J.; Desbois, G.; Urai, J. L.; Littke, R. BIB-SEM study of the pore space morphology in early mature Posidonia Shale from the Hils area, Germany. *Int. J. Coal Geol.* **2012**, *103* (0), 12−25.

(8) Houben, M. E.; Desbois, G.; Urai, J. L. A comparative study of representative 2D microstructures in Shaly and Sandy facies of Opalinus Clay (Mont Terri, Switzerland) inferred form BIB-SEM and MIP methods. *Mar. Pet. Geol.* **2014**, *49*, 143−161.

(9) Chalmers, G. R. L.; Bustin, R. M. The organic matter distribution and methane capacity of the Lower Cretaceous strata of Northeastern British Columbia, Canada. *Int. J. Coal Geol.* **2007**, *70* (1−3), 223−239.

(10) Chalmers, G. R.; Bustin, R. M.; Power, I. M. Characterization of gas shale pore systems by porosimetry, pycnometry, surface area, and field emission scanning electron microscopy/transmission electron microscopy image analyses: Examples from the Barnett, Woodford, Haynesville, Marcellus, and Doig units. *AAPG Bull.* **2012**, *96* (6), 1099−1119.

(11) Gasparik, M.; Ghanizadeh, A.; Bertier, P.; Gensterblum, Y.; Bouw, S.; Krooss, B. M. High-Pressure Methane Sorption Isotherms of Black Shales from The Netherlands. *Energy Fuels* **2012**, *26* (8), 4995−5004.

(12) Gasparik, M.; Bertier, P.; Gensterblum, Y.; Ghanizadeh, A.; Krooss, B. M.; Littke, R. Geological controls on the methane storage capacity in organic-rich shales. *Int. J. Coal Geol.* **2014**, *123*, 34−51.

(13) Keller, L. M.; Holzer, L.; Schuetz, P.; Gasser, P. Pore space relevant for gas permeability in Opalinus clay: Statistical analysis of homogeneity, percolation, and representative volume element. *J. Geophys. Res. Solid Earth* **2013**, *118* (6), 2799−2812.

(14) Busch, A.; Amann-Hildenbrand, A. Predicting capillarity of mudrocks. *Mar. Pet. Geol.* **2013**, *45*, 208−223.

(15) Van Loon, L. R.; Soler, J. M.; Müller, W.; Bradbury, M. H. Anisotropic Diffusion in Layered Argillaceous Rocks: A Case Study with Opalinus Clay. *Environ. Sci. Technol.* **2004**, *38* (21), 5721−5728.

(16) Wenk, H.-R.; Voltolini, M.; Mazurek, M.; Van Loon, L. R.; Vinsot, A. Preferred orientations and anisotropy in shales: Callovo-Oxfordian shale (France) and Opalinus Clay (Switzerland). *Clays Clay Miner.* **2008**, *56* (3), 285−306.

(17) Gu, X.; Cole, D. R.; Rother, G.; Mildner, D. F. R.; Brantley, S. L. Pores in Marcellus Shale: A Neutron Scattering and FIB-SEM Study. *Energy Fuels* **2015**, *29* (3), 1295−1308.

(18) Zachara, J.; Brantley, S.; Chorover, J.; Ewing, R.; Kerisit, S.; Liu, C.; Perfect, E.; Rother, G.; Stack, A. G. Internal Domains of Natural Porous Media Revealed: Critical Locations for Transport, Storage, and Chemical Reaction. *Environ. Sci. Technol.* **2016**, *50* (6), 2811−2829.

(19) Houben, M. E.; Desbois, G.; Urai, J. L. Pore morphology and distribution in the Shaly facies of Opalinus Clay (Mont Terri, Switzerland): Insights from representative 2D BIB−SEM investigations on mm to nm scale. *Appl. Clay Sci.* **2013**, *71*, 82−97.

(20) Keller, L. M.; Holzer, L.; Wepf, R.; Gasser, P. 3D geometry and topology of pore pathways in Opalinus clay: Implications for mass transport. *Appl. Clay Sci.* **2011**, *52* (1−2), 85−95.

(21) Keller, L. M.; Schuetz, P.; Erni, R.; Rossell, M. D.; Lucas, F.; Gasser, P.; Holzer, L. Characterization of multi-scale microstructural features in Opalinus Clay. *Microporous Mesoporous Mater.* **2013**, *170* (0), 83−94.

(22) Javadpour, F. Nanopores and Apparent Permeability of Gas Flow in Mudrocks (Shales and Siltstone). *J. Canad. Pet. Technol.* **2009**, *48* (8), 6−21.

DOI: 10.1021/acs.energyfuels.6b02256
Energy Fuels XXXX, XXX, XXX−XXX

(23) King, H. E.; Eberle, A. P. R.; Walters, C. C.; Kliewer, C. E.; Ertas, D.; Huynh, C. Pore Architecture and Connectivity in Gas Shale. *Energy Fuels* **2015**, *29* (3), 1375−1390.
(24) Klaver, J.; Desbois, G.; Urai, J. L.; Littke, R. BIB-SEM characterization of pore space morphology and distribution in postmature to overmature samples from the Haynesville and Bossier Shales. *Mar. Pet. Geol.* **2015**, *59*, 451−466.
(25) Hemes, S.; Desbois, G.; Urai, J. L.; Schröppel, B.; Schwarz, J.-O. Multi-scale characterization of porosity in Boom Clay (HADES-level, Mol, Belgium) using a combination of X-ray μ-CT, 2D BIB-SEM and FIB-SEM tomography. *Microporous Mesoporous Mater.* **2015**, *208*, 1−20.
(26) Busch, A.; Schweinar, K.; Kampman, N.; Coorn, A.; Pipich, V.; Feoktystov, A.; Leu, L.; Amann-Hildenbrand, A.; Bertier, P. Determining the porosity of mudrocks using methodological pluralism. *Geol. Soc. London Spec. Publ.* **2016**, accepted.
(27) Bertier, P.; Schweinar, K.; Stanjek, H.; Ghanizadeh, A.; Clarkson, C. R.; Busch, A.; Kampman, N.; Prinz, D.; Amann-Hildenbrand, A.; Krooss, B. M.; Pipich, V.; Di, Z. On the Use and Abuse of N2 Physisorption for the Characterisation of the Pore Structure of Shales. *Clay Min. Soc. Worksh. Lect.* **2016**, *12*, 151−161.
(28) Mastalerz, M.; He, L.; Melnichenko, Y. B.; Rupp, J. A. Porosity of Coal and Shale: Insights from Gas Adsorption and SANS/USANS Techniques. *Energy Fuels* **2012**, *26* (8), 5109−5120.
(29) Jin, L.; Mathur, R.; Rother, G.; Cole, D.; Bazilevskaya, E.; Williams, J.; Carone, A.; Brantley, S. Evolution of porosity and geochemistry in Marcellus Formation black shale during weathering. *Chem. Geol.* **2013**, *356* (0), 50−63.
(30) Bahadur, J.; Melnichenko, Y. B.; Mastalerz, M.; Furmann, A.; Clarkson, C. R. Hierarchical Pore Morphology of Cretaceous Shale: A Small-Angle Neutron Scattering and Ultrasmall-Angle Neutron Scattering Study. *Energy Fuels* **2014**, *28* (10), 6336−6344.
(31) Bahadur, J.; Radlinski, A. P.; Melnichenko, Y. B.; Mastalerz, M.; Schimmelmann, A. Small-Angle and Ultrasmall-Angle Neutron Scattering (SANS/USANS) Study of New Albany Shale: A Treatise on Microporosity. *Energy Fuels* **2015**, *29* (2), 567−576.
(32) Kampman, N.; Busch, A.; Bertier, P.; Snippe, J.; Hangx, S.; Pipich, V.; Di, Z.; Rother, G.; Harrington, J. F.; Evans, J. P.; Maskell, A.; Chapman, H. J.; Bickle, M. J. Observational evidence confirms modelling of the long-term integrity of CO2-reservoir caprocks. *Nat. Commun.* **2016**, *7*, 12268.
(33) Lee, S.; Fischer, T. B.; Stokes, M. R.; Klingler, R. J.; Ilavsky, J.; McCarty, D. K.; Wigand, M. O.; Derkowski, A.; Winans, R. E. Dehydration Effect on the Pore Size, Porosity, and Fractal Parameters of Shale Rocks: Ultrasmall-Angle X-ray Scattering Study. *Energy Fuels* **2014**, *28* (11), 6772−6779.
(34) Fratzl, P.; Jakob, H. F.; Rinnerthaler, S.; Roschger, P.; Klaushofer, K. Position-Resolved Small-Angle X-ray Scattering of Complex Biological Materials. *J. Appl. Crystallogr.* **1997**, *30* (5 Part 2), 765−769.
(35) Bunk, O.; Bech, M.; Jensen, T. H.; Feidenhans'l, R.; Binderup, T.; Menzel, A.; Pfeiffer, F. Multimodal x-ray scatter imaging. *New J. Phys.* **2009**, *11* (12), 1−8.
(36) Fonseca, D. M.; Meheust, Y.; Fossum, J. O.; Knudsen, K. D.; Parmar, K. P. S. Phase diagram of polydisperse Na-fluorohectorite-water suspensions: A synchrotron small-angle x-ray scattering study. *Phys. Rev. E* **2009**, *79* (2), 10.1103/PhysRevE.79.021402
(37) Giannini, C.; Siliqi, D.; Ladisa, M.; Altamura, D.; Diaz, A.; Beraudi, A.; Sibillano, T.; De Caro, L.; Stea, S.; Baruffaldi, F.; Bunk, O. Scanning SAXS-WAXS microscopy on osteoarthritis-affected bone—an age-related study. *J. Appl. Crystallogr.* **2014**, *47* (1), 110−117.
(38) Anovitz, L. M.; Cole, D. R.; Meyer Sheets, J.; Swift, A.; Elston, H. W.; Welch, S.; Chipera, S. J.; Littrell, K. C.; Mildner, D. F. R.; Wasbrough, M. J. Effects of maturation on multiscale (nanometer to millimeter) porosity in the Eagle Ford Shale. *Interpretation* **2015**, *3* (3), SU59−SU70.
(39) Todt, J.; Hammer, H.; Sartory, B.; Burghammer, M.; Kraft, J.; Daniel, R.; Keckes, J.; Defregger, S. X-ray nanodiffraction analysis of stress oscillations in a W thin film on through-silicon via. *J. Appl. Crystallogr.* **2016**, *49* (1), 182−187.
(40) Kanitpanyacharoen, W.; Kets, F. B.; Wenk, H.-R.; Wirth, R. Mineral preferred orientation and microstructure in the Posidonia shale in relation to different degrees of thermal maturity. *Clays Clay Miner.* **2012**, *60* (3), 315−329.
(41) Radlinski, A. P.; Boreham, C. J.; Wignall, G. D.; Lin, J. S. Microstructural evolution of source rocks during hydrocarbon generation: A small-angle-scattering study. *Phys. Rev. B: Condens. Matter Mater. Phys.* **1996**, *53* (21), 14152−14160.
(42) Anovitz, L. M.; Cole, D. R. Characterization and Analysis of Porosity and Pore Structures. *Rev. Mineral. Geochem.* **2015**, *80*, 61−164.
(43) Ciccariello, S.; Riello, P. Small-angle scattering from three-phase samples: application to coal undergoing an extraction process. *J. Appl. Crystallogr.* **2007**, *40* (2), 282−289.
(44) Radlinski, A. P.; Ioannidis, M. A.; Hinde, A. L.; Hainbuchner, M.; Baron, M.; Rauch, H.; Kline, S. R. Angstrom-to-millimeter characterization of sedimentary rock microstructure. *J. Colloid Interface Sci.* **2004**, *274* (2), 607−612.
(45) Hinde, A. PRINSAS—a Windows-based computer program for the processing and interpretation of small-angle scattering data tailored to the analysis of sedimentary rocks. *J. Appl. Crystallogr.* **2004**, *37* (6), 1020−1024.
(46) Radlinski, A. P. Small-Angle Neutron Scattering and the Microstructure of Rocks. *Rev. Mineral. Geochem.* **2006**, *63*, 363−397.
(47) Alqudah, M.; Ali Hussein, M.; van den Boorn, S.; Giraldo, V. M.; Kolonic, S.; Podlaha, O. G.; Mutterlose, J. Eocene oil shales from Jordan—Paleoenvironmental implications from reworked microfossils. *Mar. Pet. Geol.* **2014**, *52*, 93−106.
(48) https://www.psi.ch/sls/csaxs/software.
(49) Bressler, I.; Kohlbrecher, J.; Thunemann, A. F. SASfit: a tool for small-angle scattering data analysis using a library of analytical expressions. *J. Appl. Crystallogr.* **2015**, *48* (5), 1587−1598.
(50) Zhang, F.; Ilavsky, J.; Long, G. G.; Quintana, J. P. G.; Allen, A. J.; Jemian, P. R. Glassy Carbon as an Absolute Intensity Calibration Standard for Small-Angle Scattering. *Metall. Mater. Trans. A* **2010**, *41* (5), 1151−1158.
(51) http://www.fei.com/software/avizo3d/.
(52) King, H., Jr.; Milner, S. T.; Lin, M. Y.; Singh, J. P.; Mason, T. Structure and Rheology of Organoclay Suspensions. *Phys. Rev. E* **2007**, *75*, 021403−021423.

DOI: 10.1021/acs.energyfuels.6b02256
Energy Fuels XXXX, XXX, XXX−XXX